



Article

# Thermal Runaway Warning of Lithium Battery Based on Electronic Nose and Machine Learning Algorithms

**Zilong Pu** <sup>1,2</sup>, **Miaomiao Yang** <sup>1,2</sup>, **Mingzhi Jiao** <sup>1,2,3,\*</sup>, **Duan Zhao** <sup>1,2</sup>, **Yu Huo** <sup>1,2,\*</sup> and **Zhi Wang** <sup>3,4,5,\*</sup>

<sup>1</sup> School of Information and Control Engineering, China University of Mining and Technology, Xuzhou 221116, China; ts22060164p31@cumt.edu.cn (Z.P.); ts23060020a31tm@cumt.edu.cn (M.Y.); duan.zhao@cumt.edu.cn (D.Z.)

<sup>2</sup> The State and Local Joint Engineering Laboratory of Perception Mine, China University of Mining and Technology, Xuzhou 221116, China

<sup>3</sup> School of Safety Engineering, China University of Mining and Technology, Xuzhou 221116, China

<sup>4</sup> Civil Aircraft Fire Science and Safety Engineering Key Laboratory of Sichuan Province, Guanghan 618300, China

<sup>5</sup> China Academy of Safety Science and Technology, Beijing 100012, China

\* Correspondence: mingzhi.jiao@cumt.edu.cn (M.J.); yuhuo@cumt.edu.cn (Y.H.); zhiwang@cumt.edu.cn (Z.W.)

**Abstract:** Characteristic gas detection can be an efficient way to predict the degree of thermal runaway of a lithium battery. In this work, a sensor array consisting of three commercial MOS sensors was employed to discriminate between three target gases, CO, H<sub>2</sub> and a mixture of the two, which are characteristic gases released during the thermal runaway of lithium batteries. In this work, an integrated model that makes the classification stage results one of the feature inputs for the concentration regression stage was employed, successfully reducing the RMSE of the concentration regression results. In addition, we also explored the influence of the selection of the response time length on the classification and regression tasks, achieving the best results in a short time through the optimum algorithm. To assess the impact of time duration sensor data on the results, we selected four time windows of different length and extracted the corresponding sensor response data for subsequent processing. Initially, principal component analysis (PCA) was used to visualise the clustering of the three target gas samples at room temperature, providing a preliminary data analysis. For the classification phase, we chose three classification algorithms—MLP (Multilayer Perceptron), ELM (Extreme Learning Machine), and SVM (Support Vector Machine)—and performed a comprehensive comparison of their classification and generalisation abilities using grid search for hyperparameter optimisation and five-fold cross-validation. The results demonstrated that MLP achieved 99.23% classification accuracy during the 20 s response period. In the concentration regression phase, we combined the classification results with the raw features to create a new feature set, which was then input into a multi-output MLP regression model. The root mean square error (RMSE) employing the new feature set was used to measure the prediction error. Ultimately, the findings showed that the input of combined features significantly reduced the regression error for the mixed gas.



**Citation:** Pu, Z.; Yang, M.; Jiao, M.; Zhao, D.; Huo, Y.; Wang, Z. Thermal Runaway Warning of Lithium Battery Based on Electronic Nose and Machine Learning Algorithms. *Batteries* **2024**, *10*, 390. <https://doi.org/10.3390/batteries10110390>

Academic Editor: Vilas Pol

Received: 30 September 2024

Revised: 21 October 2024

Accepted: 23 October 2024

Published: 5 November 2024

**Keywords:** lithium battery; thermal runaway warning; MOS sensor; electronic nose; gas classification; concentration regression



**Copyright:** © 2024 by the authors. Licensee MDPI, Basel, Switzerland. This article is an open access article distributed under the terms and conditions of the Creative Commons Attribution (CC BY) license (<https://creativecommons.org/licenses/by/4.0/>).

## 1. Introduction

With the continuous progress of technology and the growing demand for environmentally friendly energy, lithium batteries have become one of the indispensable energy mediums in modern society. From smartphones to electric vehicles, portable electronic devices to energy storage systems, the application of lithium batteries has permeated every aspect of our lives [1,2]. However, despite their numerous advantages in energy density,

charging speed, and lifespan, the potential dangers associated with thermal runaway in lithium batteries have become increasingly prominent.

Thermal runaway in lithium batteries can lead to fires, explosions, and even personal injury. Lithium-ion batteries may fail to adhere to their intrinsic electrical properties under certain abnormal conditions—such as overcharging or over-discharging, physical damage, internal short circuits, or high-temperature environments [3–6]. This can cause thermal runaway of the electrolyte, triggering a chain reaction that releases a significant amount of heat and harmful gases [3,4], potentially leading to catastrophic outcomes. Despite a series of safety measures implemented during the design and manufacturing of lithium batteries—such as the selection of more reliable anode materials, thermal management systems, and the addition of flame retardants [5–7]—the complexity of their internal chemical characteristics and the unpredictability of external environments mean that thermal runaway remains a significant issue.

Therefore, to promote the continuous development of lithium battery technology and ensure its safety, more in-depth research and exploration are needed to prevent thermal runaway. From a regulatory perspective, the United Nations' proposed Global Technical Regulation No. 20 for Electric Vehicle Safety (EVS) requires that, in the event of thermal runaway, vehicles must provide a warning at least five minutes in advance for the evacuation of passengers from hazardous conditions.

Currently, safety monitoring technologies for commercial lithium-ion batteries primarily focus on detecting temperature rise, pressure distribution changes and impedance variations, etc. However, there is relatively little research on the analysis and early warning detection of released mixed gases. Koch et al. [8] assembled a sensor array consisting of voltage, temperature, pressure, smoke, creeping distance, expansion stress, and gas sensors to conduct thermal runaway tests on lithium battery packs of different sizes, energy densities, and configurations. The results showed that, compared to other sensors, gas sensors show the fastest and clearest response. Pressure and force sensors also responded quickly but with weaker signal amplitudes, while voltage, smoke, and creeping distance sensors required the longest response times. This further demonstrates the higher reliability and accuracy of gas sensors in the detection and early warning of battery thermal runaway. Evaluating the sensitivity and accuracy of monitoring and detecting thermal runaway using temperature, voltage, and gas sensors. It was proved that gas sensors could detect fault signals approximately 10 min before the actual occurrence of thermal runaway, which is about 2 min earlier than voltage sensors and about 7 min earlier than temperature sensors. Koch et al. [9] evaluated the gases released during thermal runaway in 51 different types of batteries, finding that seven components—CO<sub>2</sub>, CO, H<sub>2</sub>, C<sub>2</sub>H<sub>4</sub>, CH<sub>4</sub>, C<sub>2</sub>H<sub>6</sub>, and C<sub>3</sub>H<sub>6</sub>—accounted for more than 99% of the total emissions. Essl et al. [10] developed a custom battery thermal runaway reaction test bench and a gas sensitivity platform to analyse the thermal runaway process, primarily detecting CO<sub>2</sub>, CO, H<sub>2</sub>, C<sub>2</sub>H<sub>4</sub>, CH<sub>4</sub>, along with small amounts of electrolyte vapour and water. Golubkov et al. [11] analysed the gas composition during thermal runaway of 18,650 commercial batteries using three different cathode materials. Although the volume fractions of gases released varied with different materials, CO<sub>2</sub>, CO, H<sub>2</sub>, C<sub>2</sub>H<sub>4</sub>, and CH<sub>4</sub> were consistently detected.

We can utilise an electronic nose to monitor the mixed gases released during the thermal runaway of lithium batteries and achieve early warning. The electronic nose is an artificial sensor system that simulates the biological nose to detect and identify gas components. It simulates the basic principles of the human olfactory system by using an array of gas sensors to capture odours and convert them into quantifiable signals [12]. These signals can then be analysed and processed to identify the presence and concentration of specific gas components. In practical applications, electronic noses are widely used in food processing, medical diagnosis, environmental monitoring, and other fields [13–15]. Based on the research and analysis of previous related work, compared to other models, MLP, ELM, and SVM are commonly used in the classification and regression of gas sensor array data and have achieved desirable results. MLP is an artificial neural network that uses the

backpropagation method to iteratively calculate the optimal parameters for network nodes. It is widely used in the field of electronic noses. Zhang et al. [16] achieved simultaneous interference detection of CO and CH<sub>4</sub> semi-quantitatively under interfering environments using an MLP-based electronic nose model. Chu et al. [17] used a genetic algorithm-optimised MLP model to classify and identify mixtures of 11 different concentrations of nitrogen dioxide (NO<sub>2</sub>) and carbon monoxide (CO). Li et al. [18] constructed a sensor array and utilised a PSO-MLP algorithm to qualitatively identify multiple mixed toxic gases (formaldehyde, n-butanol, and isopropanol). ELM, proposed by Guang-Bin and Qin-Yu [19], is designed to train single hidden layer feedforward networks (SLFN). ELM is widely applied in electronic noses for tasks such as classification, regression, clustering, and feature mapping. Wang et al. [20] used an ELM-ELM ensemble structure to identify and predict the concentration of six VOC gases, achieving a classification accuracy of 99% and a regression R<sup>2</sup> score of 0.94. Ma et al. [21] presented a novel hierarchical classifier (HC) with a tree structure. This presented ELM-HC has demonstrated higher classification accuracy and better generalisation performance for the quantitative analysis of gases, including six toxic gases (hydrogen sulphide, carbon monoxide, ammonia, toluene, formaldehyde, acetone) and three binary gas mixtures. Ouyang et al. [22] utilised the ELM algorithm to process features from supervised learning, implementing a deep learning network for NO<sub>x</sub> concentration regression. SVM was widely employed for gas classification. Zhao et al. [23] applied SVM, BP, and ELM to identify formaldehyde in three mixed gases, with SVM achieving the best classification accuracy. Khan et al. [24] employed four supervised machine learning algorithms: Decision Tree, SVM, Naive Bayes (kernel), and k-Nearest Neighbour (k-NN) for the classification of gas type. Results indicated that the optimised SVM and NB classifier models exhibited the highest classification accuracy on the test dataset.

In this paper, we conducted data processing and analysis on the time series data collected by the sensor array in the experiment and analysed qualitatively and quantitatively the three different gases that can characterise the stage of thermal runaway. Combined with the five-fold cross-validation, we compared the classification accuracy of the three algorithms, MLP, ELM, and SVM, and combined the classification results with the raw features to obtain new combined eigenvalues. Regression accuracy is improved, and the influence of selection of different length time window data is discussed. The specific process is shown in Figure 1.

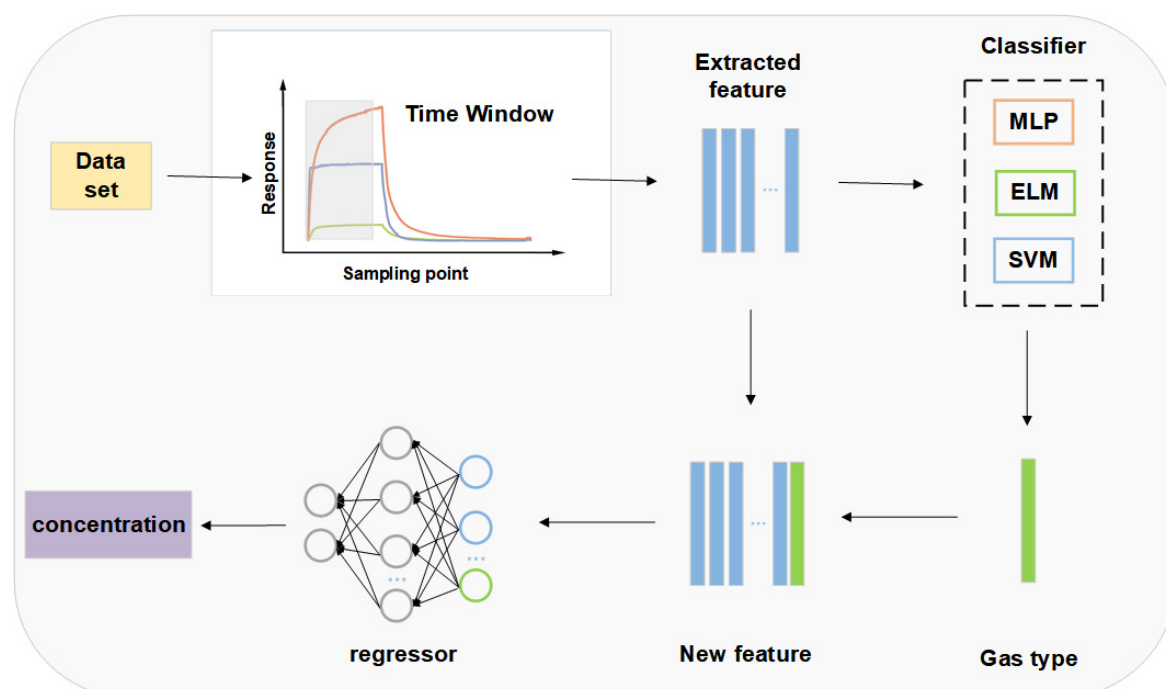


**Figure 1.** Gas classification and regression model diagram.

## 2. Experiment

### 2.1. Sensor Array

Due to the cross-sensitivity phenomenon in MOS sensors, where a single sensor may exhibit similar response patterns to different types and concentrations of gases [25], it is challenging for a single sensor to achieve precise pattern recognition. Therefore, selecting sensors with good selectivity, constructing sensor arrays, and extracting appropriate feature values are important methods to enhance selectivity.

Based on the sensor performance, cost, and power consumption, three types of commercial MOS sensors were selected to establish the sensor array. The HGS1000, HGS1001, and HGS1002 sensors used in this study were all purchased from Micro-Nano Sensing Co. LTD (Hefei, China), which are named S1, S2 and S3 below, respectively, shown in Figure 2. For MOS sensors, the physicochemical reactions between the target gases and different sensitive materials result in changes in the electrical conductivity of the sensitive materials, leading to different response patterns for different gases. Table 1 presents the target detection gases applicable to the three sensors used in this experiment and their detection ranges for the gases. All sensors are cross-sensitive to target gases, so we will train the data processing model to perform classification identification and concentration regression for different target gases.

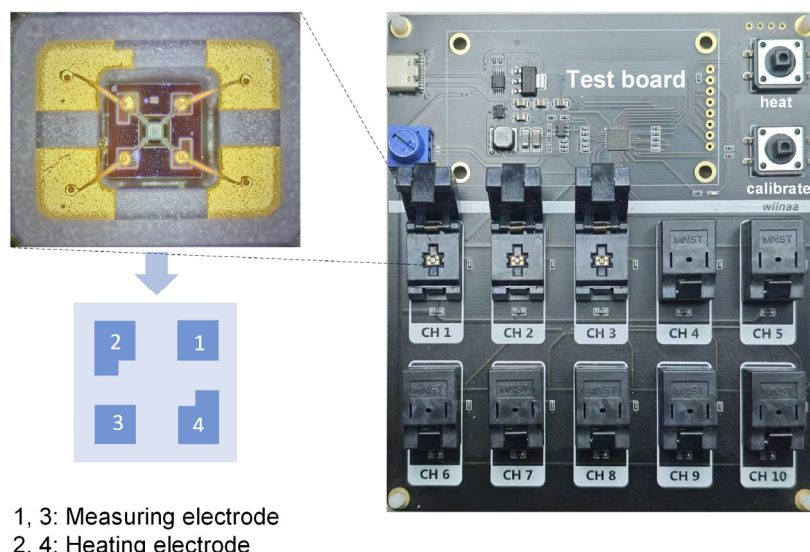


**Figure 2.** The square array plate of the detection module and MOS sensor.

**Table 1.** The selected sensor parameters.

Title 1	Sensor Type	Target Gas	Measurement Range
HGS1000	MOS	VOC, smog, etc.	1~500 ppm
HGS1001	MOS	ethanol, acetone, hydrogen, hydrogen sulfide, etc.	0.1~500 ppm
HGS1002	MOS	Ethanol, acetone, hydrogen, hydrogen sulfide, etc.	0.05~300 ppm

### 2.2. Preparation of the Samples

The experiment in this paper records the response time sequence signals of the constructed sensor array to two single gases, hydrogen and carbon monoxide, as well as their mixed gases. As demonstrated in Table 2, for the target gases in the experiment, the concentration levels for hydrogen are set to 20, 50, 100, 150, and 200 ppm. The concentration levels for carbon monoxide are set to 2, 5, 10, 15, and 20 ppm. The concentration levels for the mixed gas ( $\text{CO}, \text{H}_2$ ) are set to (18 ppm, 200 ppm), (10 ppm, 1000 ppm), and (2 ppm, 1800 ppm).

**Table 2.** Concentration settings of the Characteristic gases.

Setting No.	H <sub>2</sub> (ppm)	CO (ppm)	Total Gas (ppm)
1	20	0	20
2	50	0	50
3	100	0	100
4	150	0	150
5	200	0	200
6	0	2	2
7	0	5	5
8	0	10	10
9	0	15	15
10	0	20	20
11	200	18	218
12	1000	10	1010
13	1800	2	1802

All gas sensitivity tests throughout the work were conducted under atmospheric pressure, relative humidity of  $(60 \pm 10)\%$ , and room temperature of  $(25 \pm 2)^\circ\text{C}$ . The response of the sensor is defined as follows:

$$S = \frac{R_a}{R_g} \quad (1)$$

where  $R_a$  and  $R_g$  are the resistance of the sensor in air and target gas, respectively.

The gas sensing testing system mainly comprises three parts: the gas distribution module, the detection module, and the signal processing and pattern recognition module. The square array plate of the detection module, purchased from Micro-Nano Sensing Co. LTD, is used to collect the response signals from the sensor array at a sampling frequency of 10 Hz (ten times per second). During the experiment, the sensor array plate is placed in a test chamber with a volume of 1 L and interacts with the target gas to generate a response time sequence signal, which is transmitted to a computer for further processing.

Before testing, the working voltage of the sensor array is set to 1.8 V, and a preheating period of 24 h is conducted to ensure the stable operation of the sensor array. During the sample testing phase, standard air is first introduced into the test chamber for 30 min to clean the gas chamber, remove interferences, and ensure the stability of the sensor response baseline. Since metal oxide semiconductor sensors cannot operate without oxygen, the three target gases are mixed with standard air to different target concentrations and then introduced into the test chamber at a constant flow rate for 2.5 min to ensure complete interaction with the sensors, thereby obtaining response phase data.

After the response phase, standard air is introduced at a constant flow rate to clean the sensor array during the response recovery phase, which lasts for 5 min, resulting in a complete experimental sample. The above process is repeated ten times for each concentration to study the reproducibility of the sensors and improve the accuracy of the results. Finally, a dataset containing 130 gas samples was established.

### 2.3. Sensor Response

Figure 3a–c illustrates the response and recovery processes of sensors S1, S2, and S3, respectively, to hydrogen, carbon monoxide, and the mixed gases. As the concentration of the target gases increases during the experiment, the response values of all sensors also increase accordingly. For each target gas, sensor S3 shows the highest response. Especially at higher concentrations of hydrogen, S3's response far exceeds the other two sensors. When the hydrogen concentration increases from 20 ppm to 200 ppm, its response increases from 2.85 to 64.13. This indicates that S3 is highly sensitive to hydrogen and can be used when detecting or measuring high hydrogen concentrations is required. For hydrogen, the response of S2 is higher than that of S1. However, for carbon monoxide, the responses of all three sensors are closer, especially at lower concentrations. When dealing with mixed gases, the response values of all sensors significantly increased, with S3 showing the highest response. In summary, the sensor array demonstrates good detection performance and

cross-sensitivity characteristics for the three experimental gases. These sensors exhibit different responses to different target gases, meeting the basic requirements for sensor array selection and making them suitable for constructing a sensor array.

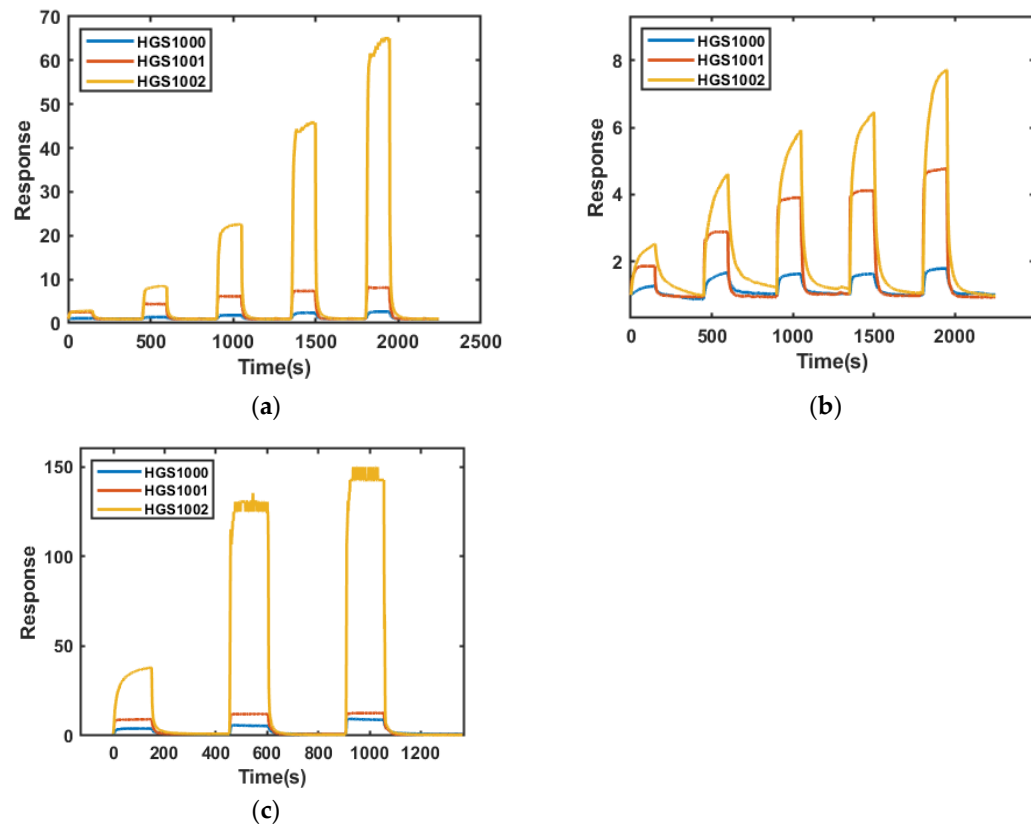


**Figure 3.** Response of sensor array to three gases: (a) H<sub>2</sub>; (b) CO; (c) the gas mixture.

### 3. Data Processing

#### 3.1. Feature Extraction

In the data processing phase, feature extraction is crucial for improving the performance of subsequent pattern recognition. Feature extraction involves processing the sensor responses to extract and select useful information. The goal is to obtain robust information with minimal redundancy from the sensor responses to ensure the effectiveness of subsequent pattern recognition algorithms. Extracting single features from the sensor array is likely to overlook the selectivity and specificity of the sensors. In this study, the integral value, first derivative, and mean value of specific response time are extracted from the original response curve of the sensor array. The first derivative represents the reaction rate of the sensor array to the gases, while the mean of the sensor response data represents the sensor's sensitivity.

These manually extracted features are then normalised, with each feature value scaled between 0 and 1. This normalisation process eliminates the impact of dimensions, reduces calculation errors, and prevents large numerical differences from affecting the accuracy of subsequent pattern recognition.

$$F' = \frac{F - F_{min}}{F_{max} - F_{min}} \quad (2)$$

#### 3.2. Data Division

During the model training process, a five-fold cross-validation method is employed. This involves randomly dividing the sample data into five mutually exclusive subsets of equal size. Each time, four subsets are used as the training set, and the remaining subset is used as the test set for model training and validation. The cross-validation process is

repeated five times, with each subset used as the test set exactly once. In total, this produces five test errors, which are averaged to generate a single estimate. This estimate is used to evaluate the model's performance under the current parameters.

### 3.3. Time Window Selection

In real-time applications, we need to perform high-precision pattern recognition of the target gas as soon as possible after the response phase begins. To evaluate the impact of time duration on the final results, feature extraction and normalisation were carried out on the data within different lengths of time windows starting from the time the gas is injected. We then use PCA (Principal Component Analysis) for visualisation and observe the clustering of samples, which aids in selecting the optimal time window length.

We classified the samples into three groups: H<sub>2</sub>, CO, and gas mixture, then used PCA to visualise the clustering of the sample data. The figure below shows 2D scatter plots of the first two principal components (PC1 and PC2) for data within the 150 s, 40 s, 20 s, and 10 s time windows after performing PCA. Since the sum of the first two principal components for each sample group explains at least 94.84% of the variance in the original data, the visualisation results of the principal component analysis are acceptable, which means clustering separation in two-dimensional space often reflects, to some extent, the clustering separation trends in high-dimensional space. In this work, we initially selected 150 s (whole response phase), 40 s, 20 s, and 10 s after the target gas injection as the time windows.

As shown in Figure 4a–c, the PCA results for the data within the 150 s, 40 s, and 20 s time windows demonstrate that while shorter time windows lead to slightly more dispersed clustering, the three target gases can still be linearly separated. However, as shown in Figure 4d, only extracting the first 10 s of response data results in noticeable overlap between samples, reducing overall accuracy. This may be because during the first 10 s of the response process, the sensitive material of the MOS sensor has not fully reacted with the target gases, resulting in a lower amount of useful information. Consequently, the sensor array's ability to distinguish between different categories and concentrations of gases is less sensitive, increasing the difficulty of subsequent pattern recognition.

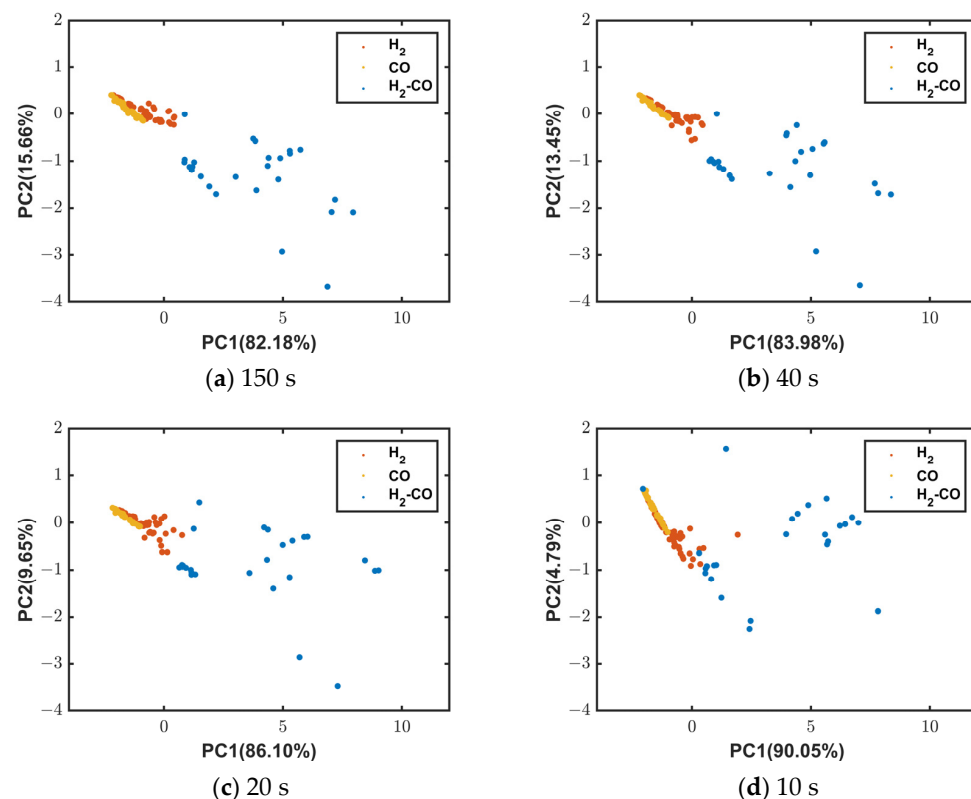


**Figure 4.** PCA result plots of data in different time windows.

## 4. Algorithm Selection

### 4.1. SVM

Support Vector Machine (SVM) is a classic supervised learning model used for classification and regression analysis. Its principle is to find a hyperplane that can be used to separate data points from different categories, the illustration of hyperplanes is shown in Figure 5. The optimal hyperplane separating the data can be obtained by solving the following optimisation problem:

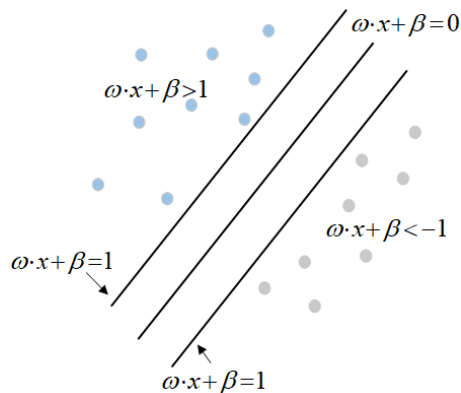


**Figure 5.** Illustration of hyperplanes.

Minimise

$$\tau(\omega) = \min_{\omega, \beta} \left\{ \frac{1}{2} \|\omega\|^2 \right\} \quad (3)$$

subject to

$$y_i((\omega \cdot x) + \beta) - 1 \geq 0 \quad (4)$$

where the vector  $\omega$  defines the boundary and  $\beta$  is a scalar threshold. In case there is an overlap between the two classes, a slack variable ( $\xi_i, i = 1, 2, \dots, k$ ) can be introduced. The optimisation problem changes as follows:

Minimise

$$\tau(\omega) = \min_{\omega, \beta} \left\{ \frac{1}{2} \|\omega\|^2 + \gamma \sum_{i=1}^k \xi_i \right\} \quad (5)$$

subject to

$$y_i((\omega \cdot x) + \beta) - 1 + \xi_i \geq 0 \quad (6)$$

where  $\gamma$  is a penalty coefficient that determines the trade-off between minimising the training error and minimising model complexity.

The four most renowned kernels are linear, polynomial, radial basis function (RBF), and sigmoid. In this work, we utilised the RBF kernel function, a commonly used high-performance function. We performed a grid search to find the optimal parameters for the regularisation parameter  $C$  and kernel coefficient  $\gamma$ . A larger penalty factor  $C$  implies a higher penalty for misclassified samples, resulting in higher accuracy on the training samples but reduced generalisation ability, meaning lower classification accuracy on the test data. Conversely, reducing  $C$  allows for some misclassification errors in the training samples, enhancing the generalisation ability.

A lower  $\gamma$  value indicates a larger radius of similarity, leading to more points being grouped together. For higher  $\gamma$  values, points need to be very close to be considered in the same group (or class). In this study, the grid search is employed to find the best parameters. Grid search involves setting a range of values for different hyperparameters and exhaustively exploring all possible combinations within that range. Cross-validation is used to evaluate the model's performance for each combination. After completing the training and test for all parameter combinations, the best combination is selected based on performance metrics (such as accuracy or F1 score), and the model is retrained using

the optimal parameters. Consequently, models with very high  $\gamma$  values tend to overfit. Therefore, we optimised  $C$  in the range of 0.01 to 100 and  $\gamma$  in the range of 0.01 to 10, with the step size set to 0.1.

#### 4.2. ELM

Extreme Learning Machine (ELM) is a training algorithm for single hidden layer feedforward neural networks (SLFN) proposed by Guang-Bin and Qin-Yu [19]. It is widely used for classification, clustering, and regression in many real-time learning tasks. ELM consists of a three-layer structure: input layer, hidden layer, and output layer, as shown in Figure 6.

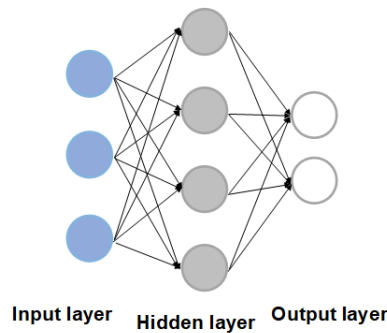


**Figure 6.** Structure of ELM.

Unlike gradient-based methods, ELM assigns random values  $\omega_i$  and  $b_i$  to the weights and biases between the input and hidden layers. The input vectors are mapped to a random feature space with randomly set and nonlinear activation functions. The nonlinear activation function in the hidden layer provides the system's nonlinearity, thus it can be considered a linear system.

The parameters between the input and hidden layers remain fixed, and the only parameters that need to be learnt are the weights between the hidden and output layers. The mathematical model of ELM is:

$$\sum_{i=1}^{\tilde{N}} \beta_i g_i(x_j) = \sum_{i=1}^{\tilde{N}} \beta_i g(\omega_i \cdot x_j + b_i) = t_j, j = 1, \dots, N \quad (7)$$

$g()$  is the activation function,  $\omega_i = \omega_{i1}, \omega_{i2}, \dots, \omega_{inT}$  is the weight vector connecting the  $i$ th hidden node and the input nodes,  $\beta_i = \beta_{i1}, \beta_{i2}, \dots, \beta_{inT}$  is the weight vector connecting the  $i$ th hidden node and the output nodes, and  $b_i$  is the bias of the  $i$ th hidden node. Given  $N$  arbitrary samples  $(X_i, t_i)$ , where  $X_i = X_{i1}, X_{i2}, \dots, X_{inT} \in R_n$ ,  $t_i = t_{i1}, t_{i2}, \dots, t_{imT} \in R_m$ .

The equation can be succinctly written as:

$$H\beta = T \quad (8)$$

The value of  $\beta$  is obtained by solving Equation (9).

$$\beta = H^{-1}T \quad (9)$$

During the testing process, the  $H$  and  $\beta$  values obtained during training are used to calculate the approximations for the test samples. We selected the sigmoid function as the activation function for the ELM and performed a grid search over the range of 0 to 500 for the number of hidden layer nodes to achieve the optimal accuracy.

#### 4.3. MLP

MLP (Multilayer Perceptron) is a classical artificial neural network consisting of an input layer, an output layer, and one or more hidden layers in a feedforward structure. The hidden layer consists of  $S$  neurons, each with  $R$  weights. These weights can be represented

in the  $S \times R$  input weight matrix  $I$ , as shown in Equation (10). The input vector  $P$  has  $R$  elements  $[p_1, p_2, \dots, p_R]^T$ , which are multiplied by  $I$ , and the resulting matrix is added to the bias vector  $b$  to form the vector  $n$ , as shown in Equation (11). The output of the hidden layer  $a$  is the result of applying the activation function  $f(\cdot)$  to  $n$ .

$$I = \begin{bmatrix} w_{1,1} & w_{1,2} & \dots & w_{1,R} \\ w_{2,1} & w_{2,2} & \dots & w_{2,R} \\ \dots & \dots & \dots & \dots \\ w_{S,1} & w_{S,2} & \dots & w_{S,R} \end{bmatrix} \quad (10)$$

$$n = I \cdot p + b \quad (11)$$

$$a = f(n) \quad (12)$$

The same operations applied in the hidden layer are used in the output layer, which consists of  $K$  neurons, with  $a$  serving as the input vector. The hyperparameters of the MLP include learning rate, number of iterations, number of layers, and hidden layer units. The activation function for the hidden layer is the Sigmoid function. For concentration regression, the activation function for the output layer is Softmax, which provides quantitative predictions for sample gases. We train the neural network using the backpropagation algorithm, allowing the model parameters to be automatically obtained without prior knowledge, regardless of the sensors or target gases.

We set the number of iterations to 1000. Additionally, since the dataset used in this study is relatively small, we set the target training error to  $1 \times 10^{-6}$  and automatically monitor the training error to prevent overfitting. If the set value is reached, the training process is terminated early. Moreover, we set the learning rate to 0.01 and two hidden layers, as illustrated in Figure 7, with a maximum of 30 neurons per layer. Each neural network is automatically trained to search for the optimal structure and parameters [26].

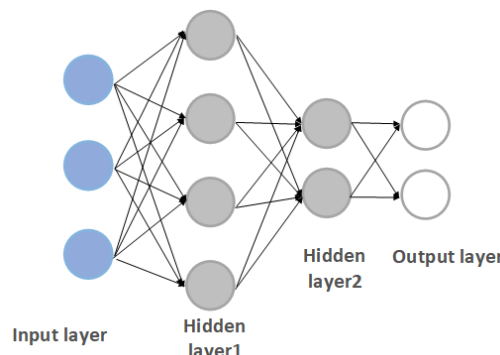


**Figure 7.** Structure of double hidden layer MLP.

## 5. Results and Discussion

### 5.1. Classification Recognition

In this study, we selected three classification models—MLP, ELM, and SVM—to train the data within different time windows. To verify the performance of the classification system, all samples were randomly shuffled, and 5-fold cross-validation and grid search hyperparameter optimisation were performed on the extracted feature data for each classification model. The optimal classification accuracy results and parameters of each algorithm for different time Windows are recorded and compared in Table 3. The confusion matrix for the classification results of data from different time windows is shown in Figure 8.

Considering the classification accuracy of the data in the 150 s time window, MLP performed the best, achieving a classification accuracy of 99.23%, as shown in Table 3. This indicates that the MLP model has the strongest fitting and generalisation abilities among the three models in this context. ELM followed with a classification accuracy of 94.62%. While ELM has certain advantages in fast learning and processing large-scale data, and it has the

fastest training and testing speed among the models, its classification accuracy is slightly lower than that of MLP. SVM had the lowest classification accuracy at 76.92%, particularly struggling with recognising mixed gas and hydrogen, with accuracies of only 73.3% and 60%, respectively. Although SVM performs well in specific problems such as small sample sizes, nonlinearity, and high-dimensional pattern recognition, its classification accuracy in this comparison was significantly lower than the other two models. The detailed confusion matrix is shown in Figure 8a–c.

The data in Table 3 also show that when the time window is shortened from 150 s to 40 s, the MLP maintains a high recognition accuracy of 99.23%, indicating that the MLP model can still provide a very high classification accuracy when processing the characteristic data in the first 40 s response stage. The classification accuracy of ELM decreased from 94.62% to 92.31%. The classification accuracy of SVM decreased slightly, from 76.92% to 75.38%. The detailed confusion matrix can be found in Figure 8d–f.

When the time window is shortened to 20 s, the classification accuracy of ELM decreases again. The classification accuracy of the MLP remained unchanged at 99.23%. Still, the number of hidden layer nodes deployed was slightly higher than that in the first two cases, and the training time increased. The classification accuracy of ELM was reduced from 92.31% to 91.54%. SVM classification accuracy barely changed, increasing slightly from 75.38% to 76.92%. This may be because SVM has reached the limit of its learning effectiveness for experimental sample data. The detailed confusion matrix can be found in Figure 8g–i.

After extracting the characteristic data of the first 10 s response stage and training the model, the best classification accuracy of MLP, ELM, and SVM is 94.61%, 88.46%, and 76.92%, respectively. Although the classification accuracy of the MLP model remained at a high level, reaching 94.61%, it decreased by 4.62% compared with the feature data extracted in the early 20 s and 40 s. This suggests that the predictive power of the MLP model may decline for features extracted within a shorter time window in the response phase. Similarly, the classification accuracy of the ELM model also decreases, reaching 88.46%, but the decline is smaller than that of MLP. The classification accuracy of the SVM model remained at 76.92%, indicating that the classification accuracy of the SVM model was not greatly affected by the data features with shorter response times. The detailed confusion matrix can be found in Figure 8j–l.

**Table 3.** Comparison of performance of the three algorithms using data within different time windows.

Time Window	Algorithm	Accuracy Rate	Hyperparameter		Time	
			Training Time (s)	Test Time (s)		
150 s	MLP	99.23%	Layer1*: 4	Layer2*: 19	$7340 \times 10^{-5}$	$320 \times 10^{-5}$
	ELM	94.62%	Layer1*: 20	-	$3.518 \times 10^{-5}$	$0.82 \times 10^{-5}$
	SVM	76.92%	C*: 62.01	$\gamma^*$ : 37.01	$19.03 \times 10^{-5}$	$6.394 \times 10^{-5}$
40 s	MLP	99.23%	Layer1: 5	Layer2: 17	$6550 \times 10^{-5}$	$345 \times 10^{-5}$
	ELM	92.31%	Layer1: 22	-	$3.588 \times 10^{-5}$	$1.136 \times 10^{-5}$
	SVM	75.38%	C: 6.01	$\gamma$ : 3.51	$18.8 \times 10^{-5}$	$6.36 \times 10^{-5}$
20 s	MLP	99.23%	Layer1: 25	Layer2: 11	$26,922 \times 10^{-5}$	$347.61 \times 10^{-5}$
	ELM	91.54%	Layer1: 30	-	$4.218 \times 10^{-5}$	$1.02 \times 10^{-5}$
	SVM	76.92%	C: 52.51	$\gamma$ : 36.51	$38.73 \times 10^{-5}$	$16.676 \times 10^{-5}$
10 s	MLP	94.61%	Layer1: 20	Layer2: 8	$23,300 \times 10^{-5}$	$338 \times 10^{-5}$
	ELM	88.46%	Layer1: 14	-	$4.24 \times 10^{-5}$	$0.656 \times 10^{-5}$
	SVM	76.92%	C: 8.51	$\gamma$ : 50.51	$20.5 \times 10^{-5}$	$7.14 \times 10^{-5}$

\* The number behind the layer is the number of neurons in that layer, C refers to regularisation parameter,  $\gamma$  refers to kernel coefficient.

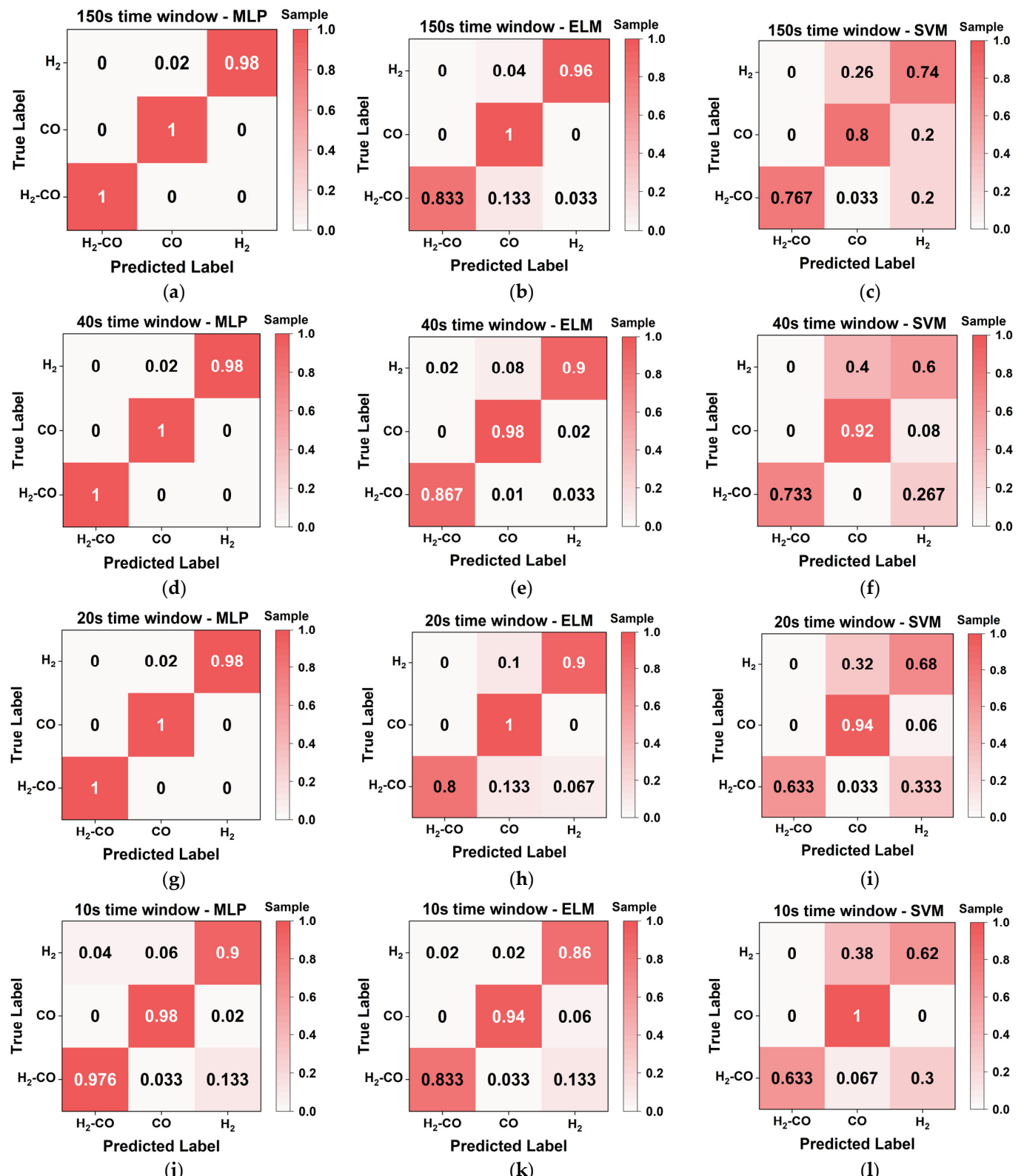


**Figure 8.** Comparison of confusion matrix of the three algorithms using 150 s data (a) MLP; (b) ELM; (c) SVM; 40 s data (d) MLP; (e) ELM; (f) SVM; 20 s data (g) MLP; (h) ELM; (i) SVM; 10 s data (j) MLP; (k) ELM; (l) SVM; where column instances are prediction class, row instances are real class.

On the whole, the classification accuracy of all models eventually decreases when the time window shortens. According to the experimental data in this paper, when the time window length is gradually shortened, MLP still maintains the best classification accuracy, indicating its high robustness to the time window length, and the classification accuracy reaches 99.23% under the 150 s, 40 s, and 20 s time windows. The classification accuracy of ELM is always slightly lower than that of MLP and is greatly affected by the length of the time window, from 94.62% to 88.46%. The classification accuracy of SVM is the lowest, only about 76%, especially for the identification of hydrogen and mixed gas. For multiclass problems, SVM needs to decompose multiclass problems into multiple binary classification problems for multiple training and prediction, which may not be as effective as other algorithms that can deal with multiclass problems. In addition, the SVM algorithm may have classification bias for datasets with unbalanced data volume.

In summary, for the classification stage, considering the high safety and efficiency requirements of the studied scenario and the fact that the accuracy of the classification stage in the integrated model affects the results of the subsequent concentration regression, we recommend training the MLP model to fit the data within the 20 s time window, which had higher recognition accuracy, as the best outcome.

## 5.2. Concentrations Regression

Considering the best fit and generalisation ability of the MLP model to the data sample in the classification stage, a multiple output MLP model was constructed to estimate the concentration of the target gas, respectively, after the classification identification stage. Two different feature inputs are selected: one is the raw features extracted in the data processing stage, and the other is the combined features of the raw feature data and the results obtained in the classification stage. The regression is fit considering the RMSE (root mean square error). The specific flowchart is demonstrated below in Figure 9 and the RMSE results with raw features and combined features as input are shown in Tables 4 and 5 respectively.

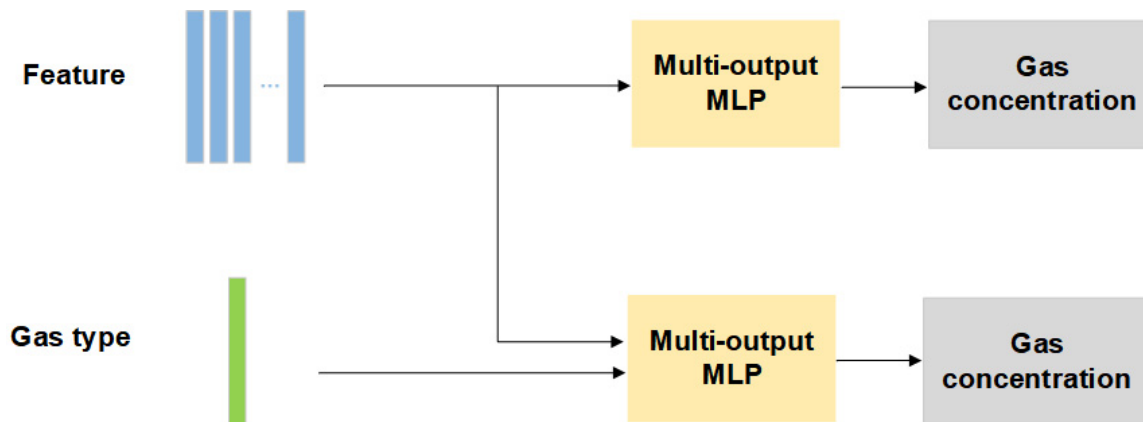


**Figure 9.** Gas concentration regression model diagram.

**Table 4.** RMSE results with raw features as input.

RMSE	150 s	40 s	20 s	10 s
H <sub>2</sub>	0.0593	0.0840	0.0790	0.1285
CO	0.1289	0.1208	0.2077	0.2916
hybrid gas	0.1208	0.1478	0.1811	0.2424

**Table 5.** RMSE results with combined features as input.

RMSE	150 s	40 s	20 s	10 s
H <sub>2</sub>	0.0537	0.0607	0.0534	0.0921
CO	0.1056	0.1156	0.1361	0.1620
hybrid gas	0.0956	0.1048	0.1137	0.1433

These data indicate the root mean square error (RMSE) of the MLP fitting results for the three gas concentrations in different time windows. RMSE is a standard index to measure the accuracy of model prediction. The lower the RMSE value, the higher the accuracy of model prediction. The RMSE trends of different gases are shown in Figure 10a–c.

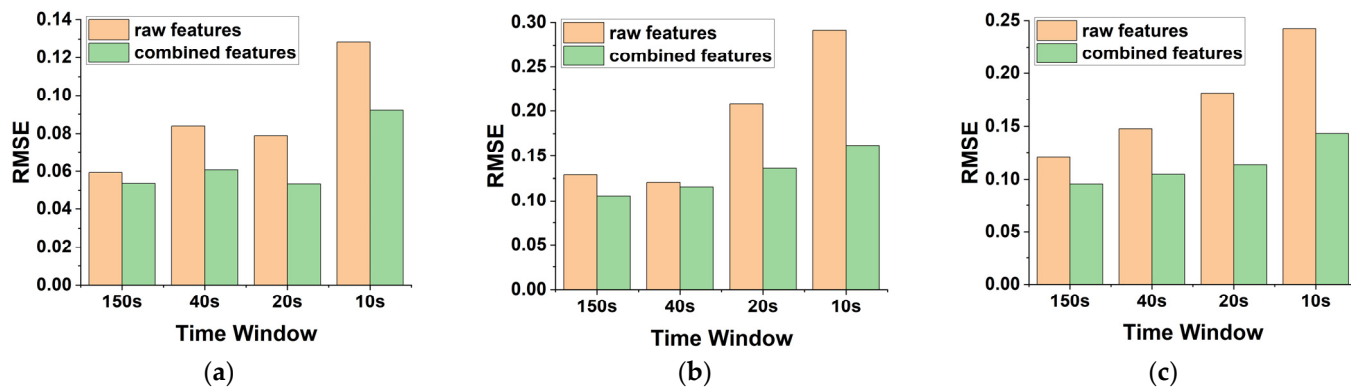


**Figure 10.** Comparison of regression results of (a) H<sub>2</sub>, (b) CO, (c) mixed gas concentration with different inputs.

From the result data, we can make the following observation: For the results of the two input features, the fitting accuracy of all gases deteriorates with the shortening of the time window (from 150 s to 10 s), and the RMSE increases, which is in line with expectations. The data information in a relatively short period may not be enough for the MLP model to accurately capture the change in gas concentration.

In the same time window, the RMSE of the combined feature input on the regression results of all gas categories decreased, indicating that the combined feature may provide better prediction information and is more suitable for the MLP model to perform the concentration regression prediction of mixed gas. Similarly, although the RMSE of the combined feature input results increases gradually with the shortening of the time range, it increases more slightly than that of the original feature. With the shortening of the time window from 150 s to 10 s, the RMSE of the mixed gas regression result of the combined feature input increased from 0.0956 to 0.1433, while that of the original feature regression results risen from 0.1208 to 0.2424.

Overall, MLP models with combined features outperformed MLP models with original features over all time ranges, especially over shorter time ranges. This may be because the combined features contain more information, which helps the model capture more complex data patterns. In addition, predictions for hydrogen are generally more accurate than those for carbon monoxide and mixed gases, which may be related to the physical properties of hydrogen or the characteristics of the dataset.

In real lithium battery thermal runaway scenarios, various background interference gases, such as CO<sub>2</sub> and C<sub>2</sub>H<sub>4</sub>, are present. The impact of these gases on the performance of our specific sensors remains to be studied. Additionally, the effects of environmental fluctuations causing noise or partial sensor failures on algorithm performance also warrant further investigation.

## 6. Conclusions

In this paper, we collected data on the responses of a sensor array to three different gases at various concentrations in the laboratory, and these three gases were identified as characteristic gases for monitoring thermal runaway in lithium-ion batteries. We also conducted classification and concentration regression of the gases. Three methods (SVM, ELM, and MLP networks) were employed to classify three types of gases. Due to mutual interference among gases in the mixture, sensor responses are not simply the mathematical sum of responses to individual gases. Among the three methods, ELM exhibited the fastest training time with high accuracy of three gases, while MLP achieved the highest

classification accuracy of three gases in 20 s. In the concentration regression stage, we used the multi-output MLP to combine the two input features and compare the root mean square error of the fitting results. The results show that the regression result of combined features is better than the original feature input effect, proving the method's feasibility.

**Author Contributions:** Conceptualization, M.J. and Z.P.; methodology, Z.P. and M.Y.; software, Z.P. and Z.W.; validation, D.Z. and Y.H.; formal analysis, Z.W.; investigation, M.J.; resources, M.J.; data curation, Z.P.; writing—original draft preparation, Z.P.; writing—review and editing, M.J.; visualisation, M.Y.; supervision, M.J.; project administration, Y.H.; funding acquisition, M.J. and D.Z. All authors have read and agreed to the published version of the manuscript.

**Funding:** This research was funded by the Department of Science and Technology of Anhui Province (2022CSJGG0703), National Natural Science Foundation of China (No. 52204253), the Opening Foundation of Civil Aircraft Fire Science and Safety Engineering Key Laboratory of Sichuan Province (MZ2023KF06), the Fundamental Research Funds for the Central Universities (2021ZDPY0208). Dr. Zhi Wang is funded by the Jiangsu Provincial Double-Innovation Doctor Program (No. 140923027), and the China Postdoctoral Science Foundation (2023M733766).

**Data Availability Statement:** The data that supported the findings of this study are available from the corresponding author upon reasonable request.

**Conflicts of Interest:** The authors declare no conflicts of interest.

## References

1. Dunn, B.; Kamath, H.; Tarascon, J.M. Electrical Energy Storage for the Grid: A Battery of Choices. *Science* **2011**, *334*, 928–935. [[CrossRef](#)] [[PubMed](#)]
2. Wang, Q.; Mao, B.; Stoliarov, S.I.; Sun, J. A review of lithium ion battery failure mechanisms and fire prevention strategies. *Prog. Energy Combust. Sci.* **2019**, *73*, 95–131. [[CrossRef](#)]
3. Fernandes, Y.; Bry, A.; de Persis, S. Identification and quantification of gases emitted during abuse tests by overcharge of a commercial Li-ion battery. *J. Power Sources* **2018**, *389*, 106–119. [[CrossRef](#)]
4. Yamanaka, T.; Takagishi, Y.; Tozuka, Y.; Yamaue, T. Modeling lithium ion battery nail penetration tests and quantitative evaluation of the degree of combustion risk. *J. Power Sources* **2019**, *416*, 132–140. [[CrossRef](#)]
5. Gao, D.; Xu, J.B.; Lin, M.; Xu, Q.; Ma, C.F.; Xiang, H.F. Ethylene ethyl phosphate as a multifunctional electrolyte additive for lithium-ion batteries. *RSC Adv.* **2015**, *5*, 17566–17571. [[CrossRef](#)]
6. Zhang, H.Y.; Pinjala, D.; Teo, P.S. Thermal management of high power dissipation electronic packages: From air cooling to liquid cooling. In Proceedings of the 5th Electronics Packaging Technology Conference (EPTC 2003), Singapore, 10–12 December 2003; pp. 620–625.
7. Zhang, S.S. A review on electrolyte additives for lithium-ion batteries. *J. Power Sources* **2006**, *162*, 1379–1394. [[CrossRef](#)]
8. Sascha, K.; Kai, B.; Robert, K. Fast Thermal Runaway Detection for Lithium-Ion Cells in Large Scale Traction Batteries. *Batteries* **2018**, *4*, 16. [[CrossRef](#)]
9. Koch, S.; Fill, A.; Birke, K.P. Comprehensive gas analysis on large scale automotive lithium-ion cells in thermal runaway. *J. Power Sources* **2018**, *398*, 106–112. [[CrossRef](#)]
10. Essl, C.; Seifert, L.; Rabe, M.; Fuchs, A. Early Detection of Failing Automotive Batteries Using Gas Sensors. *Batteries* **2021**, *7*, 25. [[CrossRef](#)]
11. Golubkov, A.W.; Fuchs, D.; Wagner, J.; Wiltsche, H.; Stangl, C.; Fauler, G.; Voitic, G.; Thaler, A.; Hacker, V. Thermal-runaway experiments on consumer Li-ion batteries with metal-oxide and olivin-type cathodes. *RSC Adv.* **2014**, *4*, 3633–3642. [[CrossRef](#)]
12. Fan, S.R.; Li, Z.; Xia, K.W.; Hao, D.X. Quantitative and Qualitative Analysis of Multicomponent Gas Using Sensor Array. *Sensors* **2019**, *19*, 3917. [[CrossRef](#)] [[PubMed](#)]
13. Chapman, E.A.; Thomas, P.S.; Stone, E.; Lewis, C.; Yates, D.H. A breath test for malignant mesothelioma using an electronic nose. *Eur. Respir. J.* **2012**, *40*, 448–454. [[CrossRef](#)] [[PubMed](#)]
14. Chen, L.Y.; Wong, D.M.; Fang, C.Y.; Chiu, C.I.; Chou, T.I.; Wu, C.C.; Chiu, S.W.; Tang, K.T. Development of an Electronic-Nose System for Fruit Maturity and Quality Monitoring. In Proceedings of the 4th IEEE International Conference on Applied System Invention (IEEE ICASI), Tokyo, Japan, 13–17 April 2018; pp. 1129–1130.
15. Men, H.; Yin, C.B.; Shi, Y.; Liu, X.T.; Fang, H.R.; Han, X.J.; Liu, J.J. Quantification of Acrylonitrile Butadiene Styrene Odor Intensity Based on a Novel Odor Assessment System With a Sensor Array. *IEEE Access* **2020**, *8*, 33237–33249. [[CrossRef](#)]
16. Zhang, J.Y.; Xue, Y.Y.; Sun, Q.Y.; Zhang, T.; Chen, Y.T.; Yu, W.J.; Xiong, Y.Z.; Wei, X.W.; Yu, G.T.; Wan, H.; et al. A miniaturized electronic nose with artificial neural network for anti-interference detection of mixed indoor hazardous gases. *Sens. Actuators B Chem.* **2021**, *326*, 128822. [[CrossRef](#)]
17. Chu, J.F.; Li, W.J.; Yang, X.; Wu, Y.; Wang, D.W.; Yang, A.J.; Yuan, H.; Wang, X.H.; Li, Y.J.; Rong, M.Z. Identification of gas mixtures via sensor array combining with neural networks. *Sens. Actuators B Chem.* **2021**, *329*, 129090. [[CrossRef](#)]

18. Li, M.H.; Ge, S.K.; Gu, Y.L.; Zhang, Y.F.; Li, X.; Zhu, H.C.; Wei, G.F. Qualitative Identification of Single/Mixture Gases Based on Fe-ZnO Sensor Array and PSO-BP Neural Network. *IEEE Sens. J.* **2023**, *23*, 20037–20043. [[CrossRef](#)]
19. Huang, G.B.; Zhu, Q.Y.; Siew, C.K. Extreme learning machine: A new learning scheme of feedforward neural networks. In Proceedings of the IEEE International Joint Conference on Neural Networks (IJCNN), Budapest, Hungary, 25–29 July 2004; pp. 985–990.
20. Wang, T.; Zhang, H.X.; Wu, Y.; Chen, X.Y.; Chen, X.W.; Zeng, M.; Yang, J.H.; Su, Y.J.; Hu, N.T.; Yang, Z. Classification and Concentration Prediction of VOCs With High Accuracy Based on an Electronic Nose Using an ELM-ELM Integrated Algorithm. *IEEE Sens. J.* **2022**, *22*, 14458–14469. [[CrossRef](#)]
21. Ma, H.L.; Wang, T.; Li, B.L.; Cao, W.Y.; Zeng, M.; Yang, J.H.; Su, Y.J.; Hu, N.T.; Zhou, Z.H.; Yang, Z. A low-cost and efficient electronic nose system for quantification of multiple indoor air contaminants utilizing HC and PLSR. *Sens. Actuators B Chem.* **2022**, *350*, 130768. [[CrossRef](#)]
22. Ouyang, T.H.; Wang, C.W.; Yu, Z.J.; Stach, R.; Mizaikoff, B.; Huang, G.B.; Wang, Q.J. NOx Measurements in Vehicle Exhaust Using Advanced Deep ELM Networks. *IEEE Trans. Instrum. Meas.* **2021**, *70*, 7000310. [[CrossRef](#)]
23. Zhao, L.; Li, X.G.; Wang, J.; Yao, P.J.; Akbar, S.A. Detection of Formaldehyde in Mixed VOCs Gases Using Sensor Array With Neural Networks. *IEEE Sens. J.* **2016**, *16*, 6081–6086. [[CrossRef](#)]
24. Khan, M.A.H.; Thomson, B.; Debnath, R.; Motayed, A.; Rao, M.V. Nanowire-Based Sensor Array for Detection of Cross-Sensitive Gases Using PCA and Machine Learning Algorithms. *IEEE Sens. J.* **2020**, *20*, 6020–6028. [[CrossRef](#)]
25. Zhou, Y.; Heng, Y.; Zhu, J.; Qian, C.; Wang, T.; Nguyen, D.H.; Jiao, M. Enhanced Gas Recognition of Electronic Nose Using 1-D Convolutional Neural Network With Savitzky–Golay Filter. *IEEE Sens. J.* **2024**, *24*, 10769–10778. [[CrossRef](#)]
26. Song, H.; Ma, L.; Pei, S.; Dong, C.; Zhu, E.; Zhang, B. Quantitative detection of formaldehyde and ammonia using a yttrium-doped ZnO sensor array combined with a back-propagation neural network model. *Sens. Actuators A Phys.* **2021**, *331*, 112940. [[CrossRef](#)]

**Disclaimer/Publisher’s Note:** The statements, opinions and data contained in all publications are solely those of the individual author(s) and contributor(s) and not of MDPI and/or the editor(s). MDPI and/or the editor(s) disclaim responsibility for any injury to people or property resulting from any ideas, methods, instructions or products referred to in the content.